INTERNATIONAL JOURNAL OF
ENERGY AND ENVIRONMENT

Volume 9, Issue 1, 2018 pp.1-26
Journal homepage: www.IJEE.IEEFoundation.org

Three-dimensional solid mechanics-CFD modeling of a PEM fuel cell stack

Maher A.R. Sadiq Al-Baghdadi

Fuel Cell Research Center, International Energy and Environment Foundation, Najaf, P.O.Box 39, Iraq.

Received 2 Jul. 2017; Received in revised form 17 Sep. 2017; Accepted 25 Sep. 2017; Available online 1 Jan. 2018

Abstract
PEM fuel cell stack assembly process, including clamping pressure, material properties of each component, design (component thickness and cell active area), and number of cells in the stack are important factors influencing the performance and durability of the PEM fuel cell stack. Furthermore, when temperature and relative humidity increase during operation, the membrane absorbs water and swells. Since the relative position between the top and bottom end plates is fixed, the polymer membrane is spatially confined. Thus the GDL will be further compressed under the land and the intrusion into channel becomes more significant. Assembly pressure, contact resistance, membrane swelling and operating conditions, etc., combine to yield an optimum assembly pressure. The clamping pressure is therefore a critical parameter for optimal fuel cell performance and durability. Too high, too low, or inhomogeneous compressions have negative effects on the performance and durability of the stack. In this study, full three-dimensional, non-isothermal computational fluid dynamics (CFD) detailed model of a PEM fuel cell stack has been developed and coupled with a solid mechanics model to simulate the stress distribution inside the stack, which are occurring during fuel cell assembly (bolt assembling), and membrane swelling and cell materials expansion during fuel cell running due to the changes of temperature and relative humidity. The PEM fuel cell stack model simulated includes the following all components in full details; two end-plates, two current plates, two bi-polar plates with straight flow channels for reactants and cooling serpentine water flow channel on the upper face of cathode bi-polar plate, two GDLs, two gaskets, and, an MEA (membrane plus two CLs). The model is shown to be able to understand the many interacting, complex electrochemical, transport phenomena, with stress distribution inside the stack during operation on the performance and durability of the stack that have limited experimental data. Furthermore, the model is shown to be able to provide a computer-aided tool for design and optimize future fuel cell stack with much higher power density, long stack life, and lower cost.

Keywords: 3D PEM fuel cell stack; CFD; Stack modeling; Mechanical analysis; Thermal stress.

1. Introduction

1.1. Durability

Durability is one of the most critical remaining issues impeding successful commercialization of broad PEM fuel cell stationary and transportation energy applications, and the durability of fuel cell stack components remains, in most cases, insufficiently understood [1-4]. Lengthy required testing times, lack

of understanding of most degradation mechanisms, and the difficulty of performing in-situ, non-destructive structural evaluation of key components makes the topic a difficult one [5, 6].
The Membrane-Electrode-Assembly (MEA) is the core component of PEM fuel cell and consists of membrane with the catalyst layers (CL) attached to each side. The fuel cell MEA durability plays a vital role in the overall lifetime achieved by a stack in field applications. Within the MEA's electrocatalyst layers are three critical interfaces that must remain properly intermingled for optimum MEA performance: platinum/carbon interface (for electron transport and catalyst support); platinum/Nafion interface (for proton transport); and Nafion/carbon interface (for high-activity catalyst dispersion and structural integrity). The MEA performance shows degradation over operating time, which is dependent upon materials, fabrication and operating conditions [7, 8].
Durability is a complicated phenomenon; linked to the chemical and mechanical interactions of the fuel cell stack components, i.e. electro-catalysts, membranes, gas diffusion layers, bipolar plates, and end plates, under severe environmental conditions, such as elevated temperature and low humidity [9]. In fuel cell systems, failure may occur in several ways such as chemical degradation of the ionomer membrane or mechanical failure in the PEM that results in gradual reduction of ionic conductivity, increase in the total cell resistance, and the reduction of voltage and loss of output power [9]. Mechanical degradation is often the cause of early life failures. Mechanical damage in the PEM can appear as through-the-thickness flaws or pinholes in the membrane, or delaminating between the polymer membrane and gas diffusion layers [1-9].
Mechanical stresses which limit MEA durability have two origins. Firstly, this is the stresses arising during fuel cell assembly (bolt assembling). The bolts provide the tightness and the electrical conductivity between the contact elements. Secondly, additional mechanical stresses occur during fuel cell running because PEM fuel cell components have different thermal expansion and swelling coefficients. Thermal and humidity gradients in the fuel cell produce dilatations obstructed by tightening of the screw-bolts. Compressive stress increasing with the hygro-thermal loading can exceed the yield strength which causes the plastic deformation. The mechanical behavior of the membrane depends strongly on hydration and temperature [1].
Water management is one of the critical operation issues in PEM fuel cells to maintain optimum water levels inside it. Spatially varying concentrations of water in both vapour and liquid form are expected throughout the cell because of varying rates of production and transport. These variations in water concentrations introduce a mechanical stresses in membrane caused by swelling/shrinking. Furthermore, high temperature and internal water flows (electroosmotic and back diffusion) can cause hot spots and local dehydration; which means that without enough water in the membrane the conductivity decays. Therefore, operation must consider appropriate measures to balance water content within the fuel cell to reduce the risk of mechanical failure and durability, consequently [2-4].
Thermal management is also required to remove the heat produced by the electrochemical reaction in order to prevent drying out of the membrane, which in turn can result not only in reduced performance but also in eventual rupture of the membrane [1-5]. Thermal management is also essential for the control of the water evaporation or condensation rates. As a result of in the changes in temperature and moisture, the PEM, gas diffusion layers (GDL), and bipolar plates will all experience expansion and contraction. Because of the different thermal expansion and swelling coefficients between these materials, hygro-thermal stresses are expected to be introduced into the unit cell during operation. In addition, the non-uniform current and reactant flow distributions in the cell can result in non-uniform temperature and moisture content of the cell, which could in turn, potentially causing localized increases in the stress magnitudes.
The need for improved lifetime of PEM fuel cells necessitates that the failure mechanisms be clearly understood and life prediction models be developed, so that new designs can be introduced to improve long-term performance. Increasing of the durability is a significant challenge for the development of fuel cell technology.

1.2. PEM fuel cell stack assembly

The stacking design and cell assembly parameters significantly affect the performance of fuel cells [10]. Adequate contact pressure is needed to hold together the fuel cell stack components to prevent leaking of the reactants, and minimize the contact resistance between layers. The required clamping force is equal to the force required to compress the fuel cell layers adequately while not impeding flow. The assembly pressure affects the characteristics of the contact interfaces between components. If inadequate or

nonuniform assembly pressure is used, there will be stack-sealing problems, such as fuel leakage, internal combustion, and unacceptable contact resistance. Too much pressure may impede flow through the GDL, or damage the MEA, resulting in a broken porous structure and a blockage of the gas diffusion passage. In both cases, the clamping pressure can decrease the cell performance. Every stack has a unique assembly pressure due to differences in fuel cell materials and stack design. Due to thin dimensions and the low mechanical strength of the electrodes and electrolyte layer versus the gaskets, bipolar plates, and end plates, the most important goal in the stack design and assembly is to achieve a proper and uniform pressure distribution [11].

The most common method of clamping the stack is by using bolts. When considering the optimal clamping pressure on the properties of the fuel cell stack, sometimes an overlooked factor is the torque required for the bolts, and the factors that contribute to the ideal torque. The optimal torque is not merely due to the ideal clamping pressure on the fuel cell layers, but it is also affected by the shape and material of the bolt and nut, the bolt seating and threading, the stack layers, thickness, and number of layers. Materials bolted together withstand moment loads by clamping the surfaces together, where the edge of the part acts as a fulcrum, and the bolt acts as a force to resist the moment created by an external force or moment [11].

The contact resistance and GDL permeability are governed by the material properties of the contacting GDL and bipolar plate layers. The contact resistance between the catalyst and membrane layers is low because they are fused together, and the contact resistance between the bipolar plates and other layers is low because the materials are typically nonporous with similar material properties (high density, with similar Poisson's ratios and Young's modulus). The GDL and the bipolar plate layers have several characteristics that make the contact resistance and permeability larger than between the other layers: (1) the Poisson's ratios and Young's modulus have large differences (a hard material with a soft material); (2) the GDL layer is porous, and the permeability has been reduced due to the reduction in pore volume or porosity; and (3) part of the GDL layer blocks the flow channels that are in the bipolar plate creating less permeability through the GDL as the compression increases [12].

1.3. PEM fuel cell stack operation

The fuel cell stack is sized to generate the designed power output. PEM fuel cells show some losses of efficiency and power density with the scale up when the number of cells and their areas increase in a stack. As fuel cell manufacturing scales up, the relationship between fuel cell performance and design, manufacturing, and assembly processes must be well understood. Assembly pressure plays a significant role in determining fuel cell performance [10, 11]. During the assembly of a PEM fuel cell stack, GDL, bipolar plate, and membrane are clamped together using mechanical devices. A proper level of clamping pressure is needed to provide adequate gas sealing, as well as to reduce contact resistances at component interfaces. However, too high a pressure may over-compress the membrane and GDL, crushing their porous structures and cracking the bipolar plate. In addition, the electrical contact resistance, which constitutes a significant part of the ohmic resistance in a cell, especially when stainless steel, titanium or molded graphite is chosen as the bipolar plate material, can be significantly altered by clamping pressure and operating conditions [13, 14]. Assembly pressure makes the part of GDL under the land area be compressed and the part under channel area be protruded into channel cavity. This inhomogeneous compression causes unevenness of the material properties of GDL. The inhomogeneous deformation of GDL as well as significant change of material properties influences fuel cell performance and durability dramatically [15].

PEM fuel cell stack assembly process, including clamping pressure, material properties of each component, design (component thickness and cell active area), and number of cells in the stack are important factors influencing the performance and durability of the PEM fuel cell stack. Furthermore, when temperature and relative humidity increase during operation, the membrane absorbs water and swells. Since the relative position between the top and bottom end plates is fixed, the polymer membrane is spatially confined. Thus the GDL will be further compressed under the land and the intrusion into channel becomes more significant [16, 17]. Assembly pressure, contact resistance, membrane swelling and operating conditions, etc., combine to yield an optimum assembly pressure.

Variations in temperature and humidity during operation cause stresses and strains (mechanical loading) in the membrane as well as in all components and are considered to be the mechanical failure driving force in fuel cell applications. Investigating the mechanical response of the PEM fuel cell stack during

operation (subjected to change in humidity and temperature) requires studying and modeling of the stress-strain behavior of all fuel cell stack components in operation phase.

1.4. State of the art

The full scale design of the PEM fuel cell stacks are quite complex. It is quite difficult and expensive to simulate the stresses distribution in the full stack. A computational model of an entire stack would require very large computing resources and excessively long simulation times. Therefore, the computational domains in the published works for the many researchers have been limited to one unit cell consist of one cathode gas flow channel and one anode gas flow channel, one cathode and one anode GDLs, and one membrane [18-30].

Most of these works were used two-dimensional assumption in their models [18-27]. However, in the two-dimensional models the hygro-thermal stresses are absent in the third direction (flow direction). The error introduced due to two-dimensional assumption is about 10% [21]. In addition, a simplified temperature and humidity profiles with no internal heat generation were assumed, (constant temperature for each upper and lower surfaces of the membrane ware assumed). The imposed moisture was also assumed to be uniformly distributed in the membrane. Uniform material properties for the membrane were also adopted. However, these questionable assumptions lead to overestimation of the maximal stresses in the membrane.

The number of papers that dealt with the mechanical simulation of the mechanical stresses in PEM fuel cells was increased. The results were more and more accurate with using three-dimensional models [28-30]. However, a simplified temperature and humidity profiles with no internal heat generation ware also assumed. In addition, constant temperature and humidity dependent material properties were utilized in the simulations for the membrane.

Al-Baghdadi [31] incorporated the effect of hygro and thermal stresses into a non-isothermal three-dimensional CFD model of PEM fuel cell to simulate the hygro and thermal stresses in the fuel cell components during running. He studied the behavior of a unit PEM fuel cell during the operation. The unit cell is consisting of a cathode and anode straight gas flow channels, GDLs, and MEA. The results showed that the displacement, deformation, and stresses have the highest values in the center of the membrane near the cathode side inlet area.

To the author's knowledge, Al-Baghdadi's work [31] is the first to incorporate the effect of mechanical and hygro-thermal stresses into actual fuel cell CFD model with three-dimensional effect. A running fuel cell has varying local conditions of temperature, humidity, and power generation (and thereby heat generation) across the active area of the fuel cell in three-dimensions. Nevertheless, except of ref. [31], no models have yet been published to incorporate the effect of hygro-thermal stresses into actual fuel cell models to study the effect of these real conditions, when cell is running, on the stresses developed in membrane and gas diffusion layers.

However, a full scale 3D analysis is required to fully encompass mechanical stresses in PEM fuel cell stacks. Full stack models must implement mainly for investigation of the mechanical stresses in PEM fuel cell stacks.

Carral and Mele [32] developed a 3D finite element model to investigate the influence of the assembly phase of PEM fuel cell stacks on the mechanical state of the active layer (MEAs). The results showed that better uniformity of the MEA compression is obtained with the greatest number of cells, and at the center of the stack. However, they not integrate stamped metallic bipolar plates due to the difficulty of the simulation.

Bates et al. [33] simulated a PEM fuel cell stack at various clamping pressures during assembly, resulting in detailed 3D plots of stress and deformation distribution in all materials of the stack. This type of simulation can be very revealing as to the effectiveness of a stack assembly. However, all components in this model are modeled as 3D objects and keep their general form, and all features have been removed from the materials except for gas channels in the bi-polar plates. They explained that the full stack analysis requires significant computing power.

Cruz et al. [34] performed a numerical simulation in order to obtain the mechanical stress distribution during assembly process for two of the most pressure sensitive components of the stack: the membrane, and the graphite plates. The stress distribution of the above mentioned components was numerically simulated by finite element analysis and the stress magnitude for the membrane was confirmed using pressure films. The analysis showed that gas inlet and outlet zones, as well as areas of the membrane in contact with rigid components require special considerations during design to avoid stress concentration.

The use of materials to dissipate the load stress and protect sensitive materials can be an alternative to maintain the integrity of the fuel cell stack and prologue its lifetime.
Charon et al. [35] suggested a numerical method towards stress calculation in a PEM fuel cell stack. A finite element model submitted to operational static load is developed for pure mechanical analysis of a stack. They applied the homogenisation technique by replacing cell parts with composite finite elements or homogenised representative elementary volumes. Then a fuel cell stack model is built and finally computed using homogenised properties. The distribution of stresses computed at stack level was applied as boundary conditions on detailed models for only a selected sensitive area to analyze local phenomena. However, their method gives good results for the calculation of stresses due to the assembly process. But as soon as the fuel cell is in operation, other physical phenomena must be considered, especially heat exchanges and the swelling of the membrane due to hydration. They concluded that finding the local stress of a stack in operation is difficult. It requires multi-physics studies, including both solid and fluid mechanics and also electrochemistry. So their work is a step towards stress calculation in a stack in operation.
Chien et al. [36] established three-dimensional finite element model of a bolted PEM fuel cell stack using the commercial software SolidWorks 2012. Then, the model was analyzed though commercial software ANSYS 15.0 while the model was subjected to different bolt pre-loadings and thermal loading. Finally, the effects of variations of bolt pre-loading on the contacting pressure, compression ratio, contact resistance, porosity and flow channel intrusion rate of GDL in a PEM fuel cell were investigated and discussed. However, in their model an internal heat resource was assumed and applied to the membrane, catalyst layers, and GDLs to simulate the generation of heat by the chemical reactions. The obtained temperature distribution was used to determine the deformation and stress of the PEM fuel cell subjected to bolt pre-loadings. In addition, the swelling of the membrane due to hydration was not considered and modeled. The hydrations have a bigger effect than temperature in developing mechanical stresses in the membrane. These stresses will be more critical when non-uniformity as a form of hydration profile across the membrane [19].
In summary, this state of the art shows that the existing models are completely based on mechanical analysis of a stack not in the case of the operating. In order to acquire a complete understanding of the damage mechanisms in the membranes and the rest of the stack components, mechanical response under hydration and thermal loads should be studied under realistic stack operating conditions.

1.5. Aim of this work

In this work, full scale three dimensional coupled solid mechanics and thermo-fluid models to predict the mechanical and hygro-thermal stresses induced during the PEM fuel cell stack assembly, and operation has been presented. The detailed swelling-thermal-structure interactions and resulting stress distributions in the stack components were addressed to improve our basic understanding of the mechanical behavior of PEM fuel cell stacks during operation.

2. PEM fuel cell stack model

The difficult experimental environment of fuel cell systems has stimulated efforts to develop models that could simulate and predict multi-dimensional coupled transport of reactants, heat and charged species using computational fluid dynamic methods. Computational Fluid Dynamics (CFD) is the science of predicting fluid flow, heat transfer, mass transfer, phase change, chemical reaction, mechanical movement, stress or deformation of related solid structures, and related phenomena by solving the mathematical equations that govern these processes using a numerical algorithm on a computer. The results of CFD analyses are relevant in: conceptual studies of new designs, detailed product development, troubleshooting, and redesign. CFD analysis complements testing and experimentation, by reduces the total effort required in the experiment design and data acquisition. CFD complements physical modeling and other experimental techniques by providing a detailed look into our fluid flow problems, including complex physical processes such as turbulence, chemical reactions, heat and mass transfer, and multiphase flows. In many cases, we can build and analyze virtual models at a fraction of the time and cost of physical modeling. This allows us to investigate more design options and "what if" scenarios than ever before. Moreover, flow modeling provides insights into our fluid flow problems that would be too costly or simply prohibitive by experimental techniques alone. The added insight and understanding gained from flow modeling gives us confidence in our design proposals, avoiding the added costs of over-sizing and over-specification, while reducing risk.

CFD modeling is a great tool for the design and analyses of fuel cell stack. The strength of the CFD numerical approach is in providing detailed insight into the various transport mechanisms and their interaction, and in the possibility of performing parameters sensitivity analyses. These models allow engineers and designers to predict the performance of the fuel cell given design parameters, material properties and operating conditions.

A PEM fuel cell stack with clamping plate and rod assembly is shown in Figure 1. The stack model simulated includes the following components; two end-plates, two current plates, two bi-polar plates, two GDLs, two gaskets, and, an MEA (membrane plus two CLs) as shown in Figure 2. Both cathode and anode have straight gas flow channels in square cross section area of 1mm. The upper face of the cathode bi-polar plate has a serpentine water flow channel in square cross section area of 2mm. Material properties and dimensions of each component are shown in Table 1.

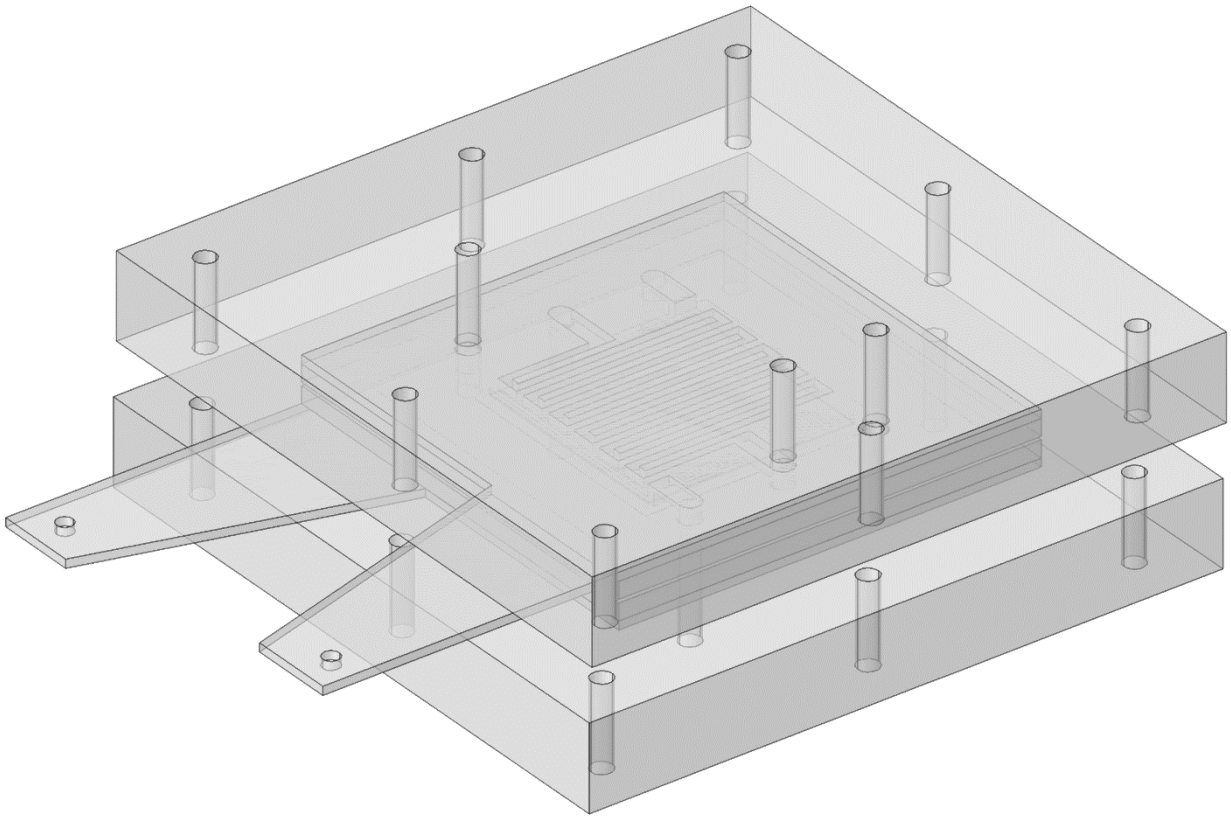

Figure 1. Three-dimensional computational domain for the PEM fuel cell stack.

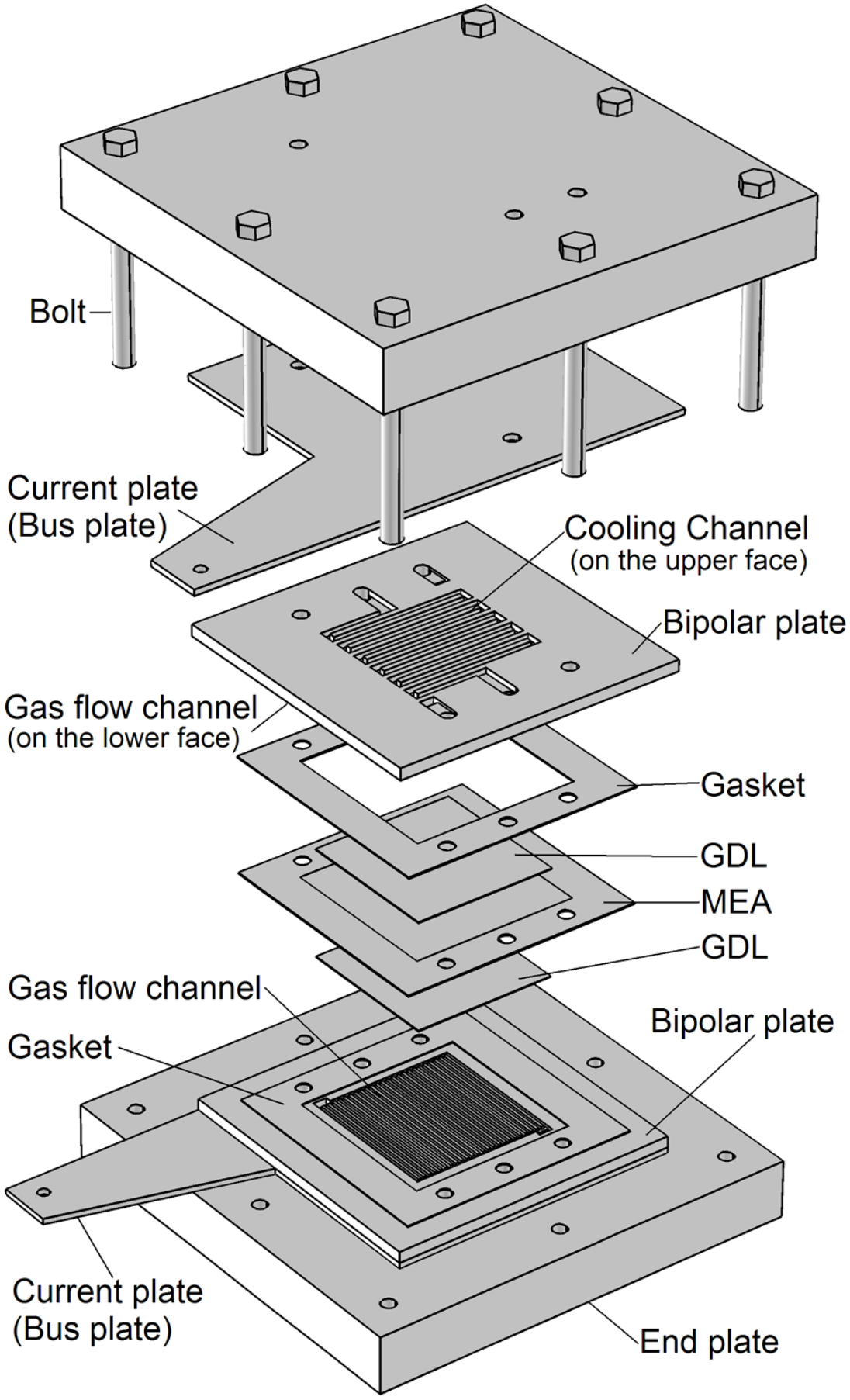

Figure 2. Description of the different stack components in computational domain.

Table 1. Properties and dimensions of the stack components.

Property	**MEA**	**GDL**	**Bipolar plate**	**Current collector**	**Gasket**	**End plate**
Material	Nafion®	Carbon paper	Carbon graphite	C15720 copper	Silicon®	Stainless steel
Young's modulus [GPa]	Table 2	10	10	110	0.54	209
Density [kg/m^3]	2000	400	1800	8700	2330	7800
Poisson's ratio	0.25	0.25	0.25	0.35	0.30	0.25
Expansion coeff. [K^{-1}]	123e^{-6}	-0.8e^{-6}	5e^{-6}	17e^{-6}	62e^{-6}	12e^{-6}
Conductivity [W m^{-1} K^{-1}]	0.455	17.122	95	385	0.517	44.5
Specific heat [J kg^{-1} K^{-1}]	1050	500	750	385	932	460
Dimensions [mm]	80 x 80	50 x 50	100 x 100	100 x 100	80 x 80	150 x 150
Thickness [mm]	0.24	0.26	4	2	0.26	20

Table 2. Young's modulus at various temperatures and humidities of Nafion®.

Young's modulus [MPa]	**Relative humidity [%]**			
	30	50	70	90
T=25 C	197	192	132	121
T=45 C	161	137	103	70
T=65 C	148	117	92	63
T=85 C	121	85	59	46

2.1. Solid mechanics model

PEM fuel cell stack assembly pressure is known to cause large strains in the stack components. All components compression occurs during the assembly process of the stack, but also during fuel cell stack operation due to membrane swelling when absorbs water and cell materials expansion due to heat generating in catalyst layers. Additionally, the repetitive channel-rib pattern of the bipolar plates results in a highly inhomogeneous compressive load, so that while large strains are produced under the rib, the region under the channels remains approximately at its initial uncompressed state. This leads to significant spatial variations in GDL thickness and porosity distributions, as well as in electrical and thermal bulk conductivities and contact resistances (both at the ribe-GDL and membrane-GDL interfaces). These changes affect the rates of mass, charge, and heat transport through the GDL, thus impacting fuel cell stack performance and lifetime.

2.1.1. Solid mechanics model during assembly

The mechanical strain induced in the components by the stacking and clamping process (assembly process) can be written from Hooke's law as [4, 5, 31];

$$\pi_M = \frac{1+\upsilon}{E}\sigma_{ij} - \frac{\upsilon}{E}\delta_{ij}\sigma_{kk} \tag{1}$$

where E is Young's modulus, υ is the Poisson's ratio of the material, δ_{ij} denotes the Kronecker delta, σ_{ij} is the stress tensor, and $\sigma_{kk} = \sigma_{11} + \sigma_{22} + \sigma_{33}$.

2.1.2. Solid mechanics model during operation

When running fuel cell stack, temperature and humidity are play critical factors in fuel cell durability. Additional mechanical stresses occur during fuel cell stack running because PEM fuel cell stack components have different thermal expansion and swelling coefficients. Thermal and humidity gradients in the fuel cell produce dilatations obstructed by tightening of the screw-bolts.

The thermal strains resulting from a change in temperature of an unconstrained isotropic volume are given by [4, 31];

$$\pi_T = \wp\left(T - T_{\mathrm{Re}f}\right) \tag{2}$$

where $\wp$ is thermal expansion [1/K].

The swelling strains caused by moisture change in membrane are given by [31];

$$\pi_S = \lambda_{mem}\left(\Re - \Re_{\mathrm{Re}f}\right) \tag{3}$$

where λ_{mem} is membrane humidity swelling-expansion and $\Re$ is the relative humidity [%].

2.2. Thermal-fluid model

2.2.1 Gas flow channels

In the fuel cell channels, the gas-flow field is obtained by solving the steady-state Navier-Stokes equations, i.e. the continuity equation, the mass conservation equation for each phase yields the volume fraction (r) and along with the momentum equations the pressure distribution inside the channels. The continuity equation for the gas phase inside the channel is given by [1-4];

$$\nabla\cdot\left(r_g\rho_g\mathbf{u}_g\right)=0 \tag{4}$$

and for the liquid phase inside the channel becomes;

$$\nabla\cdot\left(r_l\rho_l\mathbf{u}_l\right)=0 \tag{5}$$

where $\mathbf{u}$ is velocity vector [m/s], ρ is density [kg/m^3].

Two sets of momentum equations are solved in the channels, and they share the same pressure field. Under these conditions, it can be shown that the momentum equations becomes [1-4, 31];

$$\nabla\cdot\left(\rho_g\mathbf{u}_g\otimes\mathbf{u}_g-\mu_g\nabla\mathbf{u}_g\right)=-\nabla r_g\left(P+\frac{2}{3}\mu_g\nabla\cdot\mathbf{u}_g\right)+\nabla\cdot\left[\mu_g\left(\nabla\mathbf{u}_g\right)^T\right] \tag{6}$$

$$\nabla\cdot\left(\rho_l\mathbf{u}_l\otimes\mathbf{u}_l-\mu_l\nabla\mathbf{u}_l\right)=-\nabla r_l\left(P+\frac{2}{3}\mu_l\nabla\cdot\mathbf{u}_l\right)+\nabla\cdot\left[\mu_l\left(\nabla\mathbf{u}_l\right)^T\right] \tag{7}$$

where P is pressure [Pa], μ is viscosity [kg/(m·s)].

The mass balance is described by the divergence of the mass flux through diffusion and convection. Multiple species are considered in the gas phase only, and the species conservation equation in multi-component, multi-phase flow can be written in the following expression for species i [1];

$$\nabla\cdot\begin{bmatrix}-r_g\rho_g y_i\sum_{j=1}^{N}D_{ij}\frac{M}{M_j}\left[\left(\nabla y_j+y_j\frac{\nabla M}{M}\right)+\left(x_j-y_j\right)\frac{\nabla P}{P}\right]+\\ r_g\rho_g y_i\cdot\mathbf{u}_g+D_i^T\frac{\nabla T}{T}\end{bmatrix}=0 \tag{8}$$

where T is temperature (K), y is mass fraction, x is mole fraction, D is diffusion coefficient [m^2/s]. Subscript i denote oxygen at the cathode side and hydrogen at the anode side, and j is water vapour in both cases. Nitrogen is the third species at the cathode side.

The Maxwell-Stefan diffusion coefficients of any two species are dependent on temperature and pressure. They can be calculated according to the empirical relation based on kinetic gas theory [1,31];

$$D_{ij} = \frac{T^{1.75} \times 10^{-3}}{P\left[\left(\sum_k V_{ki}\right)^{1/3} + \left(\sum_k V_{kj}\right)^{1/3}\right]^2}\left[\frac{1}{M_i} + \frac{1}{M_j}\right]^{1/2} \tag{9}$$

In this equation, the pressure is in atm and the binary diffusion coefficient D_{ij} is in [cm^2/s]. The values for $\left(\sum V_{ki}\right)$ are given by Fuller et al., see ref. [1].

The temperature field is obtained by solving the convective energy equation;

$$\nabla \cdot \left(r_g\left(\rho_g Cp_g \mathbf{u}_g T - k_g \nabla T\right)\right) = 0 \tag{10}$$

where *Cp* is specific heat capacity [J/(kg.K)], k is gas thermal conductivity [W/(m.K)].

The gas phase and the liquid phase are assumed to be in thermodynamic equilibrium; hence, the temperature of the liquid water is the same as the gas phase temperature.

2.2.2 Gas diffusion layers

The physics of multiple phases through a porous medium is further complicated here with phase change and the sources and sinks associated with the electrochemical reaction. The equations used to describe transport in the gas diffusion layers are given below. Mass transfer in the form of evaporation $\left(\dot{m}_{phase} > 0\right)$ and condensation $\left(\dot{m}_{phase} < 0\right)$ is assumed, so that the mass balance equations for both phases are [1, 31];

$$\nabla \cdot \left((1 - sat)\rho_g \varepsilon \mathbf{u}_g\right) = \dot{m}_{phase} \tag{11}$$

$$\nabla \cdot \left(sat.\rho_l \varepsilon \mathbf{u}_l\right) = \dot{m}_{phase} \tag{12}$$

where *sat* is saturation, ε is porosity

The momentum equation for the gas phase reduces to Darcy's law, which is, however, based on the relative permeability for the gas phase (*Kp*). The relative permeability accounts for the reduction in pore space available for one phase due to the existence of the second phase [1, 31].

The momentum equation for the gas phase inside the gas diffusion layer becomes;

$$\mathbf{u}_g = -(1 - sat)Kp.\nabla P / \mu_g \tag{13}$$

where *Kp* is hydraulic permeability [m^2].

Two liquid water transport mechanisms are considered; shear, which drags the liquid phase along with the gas phase in the direction of the pressure gradient, and capillary forces, which drive liquid water from high to low saturation regions [37]. Therefore, the momentum equation for the liquid phase inside the gas diffusion layer becomes;

$$\mathbf{u}_l = -\frac{KP_l}{\mu_l}\nabla P + \frac{KP_l}{\mu_l}\frac{\partial P_c}{\partial sat}\nabla sat \tag{14}$$

where P_c is capillary pressure [Pa].

The functional variation of capillary pressure with saturation is prescribed following Leverett [37] who has shown that;

$$P_c = \tau\left(\frac{\varepsilon}{KP}\right)^{1/2}\left(1.417(1 - sat) - 2.12(1 - sat)^2 + 1.263(1 - sat)^3\right) \tag{15}$$

where τ is surface tension [N/m].

The liquid phase consists of pure water, while the gas phase has multi components. The transport of each species in the gas phase is governed by a general convection-diffusion equation in conjunction which the Stefan-Maxwell equations to account for multi species diffusion;

$$\nabla\cdot\begin{bmatrix}-(1-sat)\rho_g\varepsilon y_i\sum_{j=1}^{N}D_{ij}\frac{M}{M_j}\left[\left(\nabla y_j+y_j\frac{\nabla M}{M}\right)+\left(x_j-y_j\right)\frac{\nabla P}{P}\right]+\\(1-sat)\rho_g\varepsilon y_i\cdot\mathbf{u}_g+\varepsilon D_i^T\frac{\nabla T}{T}\end{bmatrix}=\dot{m}_{phase} \tag{16}$$

In order to account for geometric constraints of the porous media, the diffusivities are corrected using the Bruggemann correction formula [1, 31, 37];

$$D_{ij}^{eff}=D_{ij}\times\varepsilon^{1.5} \tag{17}$$

The heat transfer in the gas diffusion layers is governed by the energy equation as follows [1, 31, 37];

$$\nabla\cdot\left((1-sat)\left(\rho_g\varepsilon Cp_g\mathbf{u}_gT-k_{eff,g}\varepsilon\nabla T\right)\right)=\varepsilon\beta\left(T_{solid}-T\right)-\varepsilon\dot{m}_{phase}\Delta H_{evap} \tag{18}$$

where k_{eff} is effective electrode thermal conductivity [W/(m·K)]; the term [$\varepsilon\beta(T_{solid}-T)$], on the right hand side, accounts for the heat exchange to and from the solid matrix of the GDL. The gas phase and the liquid phase are assumed to be in thermodynamic equilibrium, i.e., the liquid water and the gas phase are at the same temperature.

The potential distribution in the gas diffusion layers is governed by [31];

$$\nabla\cdot\left(\lambda_e\nabla\phi\right)=0 \tag{19}$$

where λe is electrode electronic conductivity [S/m].

In order to account for the magnitude of phase change inside the GDL, expressions are required to relate the level of over- and undersaturation as well as the amount of liquid water present to the amount of water undergoing phase change.

In the case of ***evaporation***, such relations must be dependent on (i) the level of undersaturation of the gas phase in each control volume and on (ii) the surface area of the liquid water in the control volume. The surface area can be assumed proportional to the volume fraction of the liquid water in each cell. A plausible choice for the shape of the liquid water is droplets, especially since the catalyst area is Teflonated [1, 37].

The evaporation rate of a droplet in a convective stream depends on the rate of under saturation, the surface area of the liquid droplet, and a (diffusivity dependent) mass-transfer coefficient. The mass flux of water undergoing evaporation in each control volume can be represented by [37];

$$\dot{m}_{evap}=M_{H_2O}\,\varpi\,N_D\,k_{xm}\,\pi\,D_{drop}\frac{x_{w0}-x_{w\infty}}{1-x_{w0}} \tag{20}$$

where D_{drop} is Diameter of droplet water [m], k_{xm} is Mass transfer coefficient [mol/(m^2.s)], N_D is number of droplets, ϖ is Scaling parameter for evaporation.

The bulk concentration $x_{w\infty}$ is known by solving the continuity equation of water vapor. To obtain the concentration at the surface x_{w0}, it is reasonable to assume thermodynamic equilibrium between the liquid phase and the gas phase at the interface, i.e., the relative humidity of the gas in the immediate vicinity of the liquid is 100%. Under that condition, the surface concentration can be calculated based on the saturation pressure and is only a function of temperature.

The heat-transfer coefficient for convection around a sphere is well established, and by invoking the analogy between convective heat and mass transfer, the following mass-transfer coefficient was obtained by Berning and Djilali [37];

$$k_{xm} = \frac{c_{air} D_{H_2O}}{D_{drop}} \left[2 + 0.6 \left(\frac{D_{drop} v_\infty \rho_g}{\mu_g} \right)^{1/2} \left(\frac{\mu_g}{\rho_g D_{H_2O}} \right)^{1/3} \right] \tag{21}$$

It is further assumed that all droplets have a specified diameter D_{drop}, and the number of droplets in each control volume is found by dividing the total volume of the liquid phase in each control volume by the volume of one droplet;

$$N_D = \frac{sat.V_{cv}}{\frac{1}{6}\pi D_{drop}^3} \tag{22}$$

In the case when the calculated relative humidity in a control volume exceeds 100%, condensation occurs and the evaporation term is switched off.

The case of ***condensation*** is more complex, because it can occur on every solid surface area, but the rate of condensation can be different when it takes place on a wetted surface. In addition, the overall surface area in each control volume available for condensation shrinks with an increasing amount of liquid water present. Berning and Djilali [37] assumed that the rate of condensation depends only on the level of oversaturation of the gas phase multiplied by a condensation constant. Thus, the mass flux of water undergoing condensation in each control volume can be represented by;

$$\dot{m}_{cond} = \varpi \, C \frac{x_{w0} - x_{w\infty}}{1 - x_{w0}} \tag{23}$$

where C is condensation constant.

2.2.3 Catalyst layers

The catalyst layer is treated as a thin interface, where sink and source terms for the reactants are implemented. Due to the infinitesimal thickness, the source terms are actually implemented in the last grid cell of the porous medium. At the cathode side, the sink term for oxygen is given by [1, 31];

$$S_{O_2} = -\frac{M_{O_2}}{4F} i_c \tag{24}$$

where F is Faraday's constant (96487 [C/mole]), i_c is cathode local current density [A/m^2], M is molecular weight [kg/mole].

Whereas the sink term for hydrogen is specified as;

$$S_{H_2} = -\frac{M_{H_2}}{2F} i_a \tag{25}$$

where i_a is anode local current density [A/m^2]

The production of water is modelled as a source terms, and hence can be written as;

$$S_{H_2O} = \frac{M_{H_2O}}{2F} i_c \tag{26}$$

The generation of heat in the cell is due to entropy changes as well as irreversibility's due to the activation overpotential [1, 3, 31];

$$\dot{q} = \left[\frac{T(-\Delta s)}{n_e F} + \eta_{act} \right] i \tag{27}$$

where $\dot{q}$ is heat generation [W/m^2], n_e is number of electrons transfer, s is specific entropy [J/(mole.K)], η_{act} is activation overpotential (V).

The local current density distribution in the catalyst layers is modelled by the Butler-Volmer equation [1, 38, 39];

$$i_c = i_{o,c}^{ref} \left(\frac{C_{O_2}}{C_{O_2}^{ref}} \right) \left[\exp\left(\frac{\alpha_a F}{RT} \eta_{act,c} \right) + \exp\left(-\frac{\alpha_c F}{RT} \eta_{act,c} \right) \right] \tag{28}$$

$$i_a = i_{o,a}^{ref} \left(\frac{C_{H_2}}{C_{H_2}^{ref}} \right)^{1/2} \left[\exp\left(\frac{\alpha_a F}{RT} \eta_{act,a} \right) + \exp\left(-\frac{\alpha_c F}{RT} \eta_{act,a} \right) \right] \tag{29}$$

where C_{H_2} is local hydrogen concentration [mole/m3], $C_{H_2}^{ref}$ is reference hydrogen concentration [mole/m^3], C_{O_2} is local oxygen concentration [mole/m3], $C_{O_2}^{ref}$ is reference oxygen concentration [mole/m^3], $i_{o,a}^{ref}$ is anode reference exchange current density, $i_{o,c}^{ref}$ is cathode reference exchange current density, R is universal gas constant (8.314 [J/(mole·K)]), α_a is charge transfer coefficient, anode side, and α_c is charge transfer coefficient, cathode side.

2.2.4 Membrane

The balance between the electro-osmotic drag of water from anode to cathode and back diffusion from cathode to anode yields the net water flux through the membrane [1, 3, 4];

$$N_W = n_d M_{H_2O} \frac{i}{F} - \nabla \cdot \left(\rho D_W \nabla c_W \right) \tag{30}$$

where N_w is net water flux across the membrane [kg/(m^2·s)], n_d is electro-osmotic drag coefficient.

The water diffusivity in the polymer can be calculated as follow [1, 3, 31];

$$D_W = 1.3 \times 10^{-10} \exp\left[2416 \left(\frac{1}{303} - \frac{1}{T} \right) \right] \tag{31}$$

The variable c_W represents the number of water molecules per sulfonic acid group (i.e. $\text{mol}\, H_2O / \text{equivalent}\, SO_3^{-1}$). The water content in the electrolyte phase is related to water vapour activity via [1];

$$\begin{aligned} c_W &= 0.043 + 17.81a - 39.85a^2 + 36.0a^3 && (0 < a \le 1) \\ c_W &= 14.0 + 1.4(a-1) && (1 < a \le 3) \\ c_W &= 16.8 && (a \ge 3) \end{aligned} \tag{32}$$

The water vapour activity a given by;

$$a = x_W P / P_{sat} \tag{33}$$

Heat transfer in the membrane is governed by;

$$\nabla \cdot \left(k_{mem} \cdot \nabla T \right) = 0 \tag{34}$$

where k_{mem} is membrane thermal conductivity [W/(m·K)].

The potential loss in the membrane is due to resistance to proton transport across membrane, and is governed by [1, 3, 31];

$$\nabla \cdot \left(\lambda_m \nabla \phi \right) = 0 \tag{35}$$

where λ_m is membrane ionic conductivity [S/m].

The membrane type is Nafion®. Bernardi and Verbrugge [1] developed the following theoretical expression for the electric conductivity of the fully humidified membrane;

$$\lambda_m = \frac{F^2}{RT} . Z_f . D_H^+ . C_f \tag{36}$$

where Z_f is Fixed-site charge, D_H^+ is Protonic diffusion coefficient [m^2/s], C_f is Fixed charge concentration [mol/m^3].

2.3. Modeling parameters

Choosing the right modeling parameters is important in establishing the base case validation of the model against experimental results. Since the fuel cell stack model that is presented in this study accounts for all basic transport phenomena simply by virtue of its three-dimensionality, a proper choice of the modeling parameters will make it possible to obtain good agreement with experimental results obtained from a real fuel cell stack. It is important to note that because this model accounts for all major transport processes and the modeling domain comprises all the elements of a complete fuel cell stack, no parameters needed to be adjusted in order to obtain physical results.

The assembly conditions are set to reference temperature 20 C, and relative humidity 30%, where the thermal strain of the all stack components and the swelling strain of the membrane are equals to zero. The clamping forces of the nut and bolt are applied on a specific area of the end plates in the assembly procedure. The assembly was clamped together with eight bolts. The model presented in this work takes more factors into consideration during assembly such as thread pitch, bolt diameter, and friction factors. A friction factor of 0.2 is used with a torque of 5 N.m which is equivalent to a 5000 N axial load per bolt. The cell operates at a nominal current density of 1.2 A/cm^2. The selection of relatively high current density is due to illustrate the phase change effects, membrane swelling and thermal stresses which are more visible in the stack in the high loading conditions. Values of the operating conditions and electrochemical transport parameters are listed in Table 3. The governing equations were discretized using a finite-volume method and solved using a multi-physics computational fluid dynamic (CFD) code. Stringent numerical tests were performed to ensure that the solutions were independent of the grid size. A computational quadratic mesh consisting of a total of 939212 domain elements, 209214 boundary elements, and 20443 edge elements was found to provide sufficient spatial resolution (Figure 3). The coupled set of equations was solved iteratively, and the solution was considered to be convergent when the relative error was less than 1.0×10^{-6} in each field between two consecutive iterations.

Table 3. Operating conditions and electrochemical transport parameters [1].

Parameter	**Symbol**	**Value**
Air pressure (Cathode pressure) [atm]	P_c	3
Fuel pressure (Anode pressure) [atm]	P_a	3
Air stoichiometric flow ratio	ξ_c	2
Fuel stoichiometric flow ratio	ξ_a	2
Relative humidity of inlet air [%]	$\Re_c$	100
Relative humidity of inlet fuel [%]	$\Re_a$	100
Ambient temperature [K]	T_{amb}	298.15
Air inlet temperature [K]	T_{cell}	353.15
Fuel inlet temperature [K]	T_{cell}	353.15
Inlet Oxygen/Nitrogen ratio	ψ	0.79/0.21
Hydrogen reference mole fraction	$x_{H_2}^{ref}$	0.84639
Oxygen reference mole fraction	$x_{O_2}^{ref}$	0.17774
Electrode initial porosity	ε	0.4
Electrode electronic conductivity	λ_e	100 S/m
Membrane ionic conductivity (Nafion®117)	λ_m	17.1223 S/m
Transfer coefficient, anode side	α_a	0.5
Transfer coefficient, cathode side	α_c	1
Cathode reference exchange current density	$i_{o,c}^{ref}$	1.8081e^{-3} A/m^2
Anode reference exchange current density	$i_{o,a}^{ref}$	2465.598 A/m^2
Electrode thermal conductivity	k_{eff}	1.3 W/m.K
Membrane thermal conductivity	k_{mem}	0.455 W/m.K
Electrode hydraulic permeability	kp	1.76e^{-11} m^2
Entropy change of cathode side reaction	ΔS	-326.36 J/mol.K
Heat transfer coef. between solid and gas phase	β	4e6 W/m^3
Protonic diffusion coefficient	D_{H^+}	4.5e^{-9} m^2/s
Fixed-charge concentration	c_f	1200 mol/m^3
Fixed-site charge	z_f	-1
Electro-osmotic drag coefficient	n_d	2.5
Droplet diameter	D_{drop}	1e^{-8} m
Condensation constant	C	1e^{-5}
Scaling parameter for evaporation	ϖ	0.01

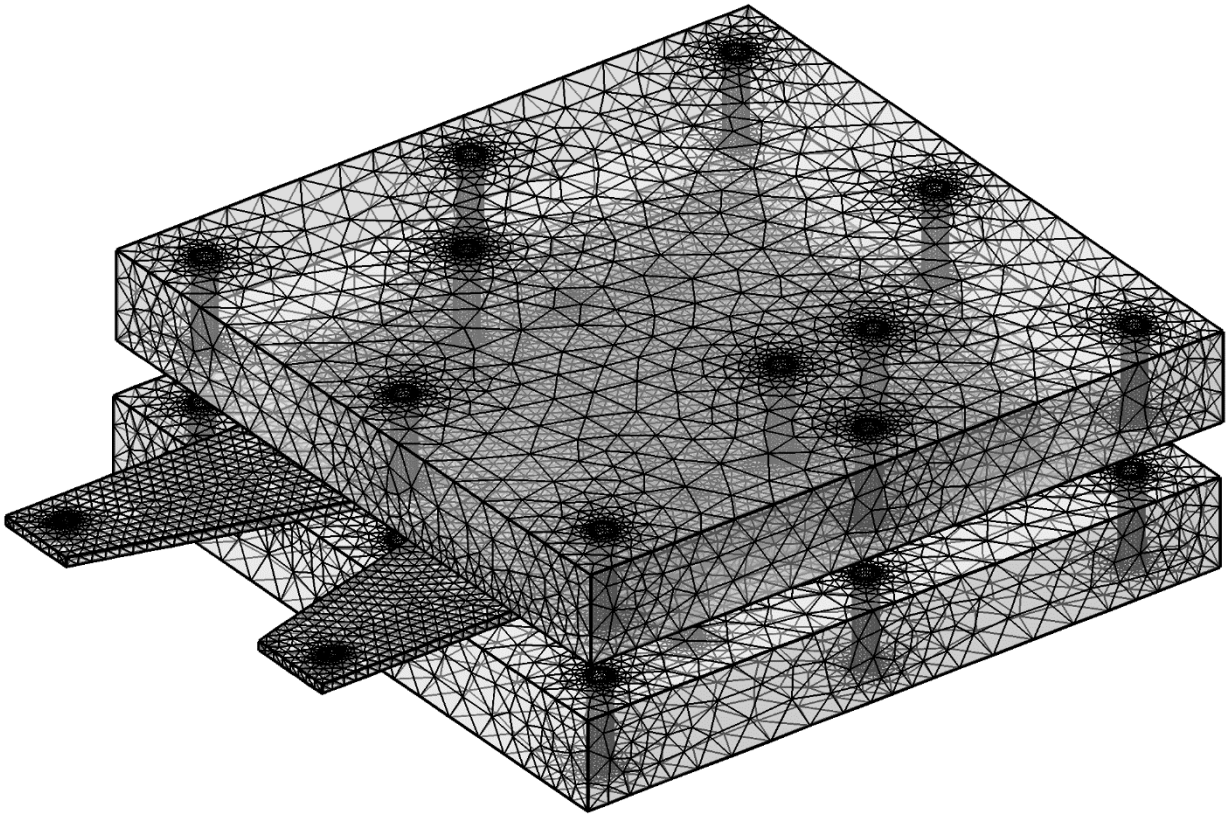

Figure 3. Computational mesh of a PEM fuel cell stack.

3. Results and discussion

The use of the CFD allows the study of the physical phenomenon within a fuel cell stack such as heat and energy transport without the need to build a structure, eliminating the manufacture and machining costs. The 3D model enables the prediction of the distribution and visualization of various parameters influencing the stack behavior .

Figure 4 represents the temperature within the different components of the stack. It is seen that the highest temperature is located close to the cathode catalyst layer, implying that major heat generation takes place in this region. The temperature over the two bipolar plates is quite uniform with one peaks coming from the heat production within the MEA (mainly within cathode side reaction layers). Overall, the temperature within the center of the stack is 8°C higher than the mean operating temperature of 80°C. Along with the figure, the temperature distribution decreases from inside to the outside walls due to heat flow to the ambient temperature. It is seen that the boundary temperature is lowest (close to 78°C) at the bipolar plates, current collectors, and end plates boundaries due to the large temperature difference (heat loss towards the surroundings).

The PEM fuel cell stack is a sandwich-like structure composed of many layers, materials and interfaces. The pressure distribution in PEM fuel cell stack therefore is affected by the component material properties, geometrical parameters and the clamping method. Figure 5 shows the total displacement distribution with a maximum value near the edges in the PEM fuel cell stack during assembly process and also during operation. The centre of the electrode tends to un-displacement. This un-displacement area increases by increasing the clamping torque. This effect confirms the hypothesis of plate deformation during the tightening. Furthermore, Figure 5 shows high deformations in the stack components during operation. This is due to the more pressure producing from the thermal expansion of the stack components materials and membrane swelling during operation with a fixed relative position between the top and bottom end plates.

In PEM fuel cells stack, all components are generally assembled between clamping plates by applying a torque moment on the tightening bolts; as a consequence the clamping force plays an important role for stack realization. The function of the stack-compression hardware is to fasten cell components with a defined and homogeneous pressure. If these requirements are not accurately fulfilled, the function and

the durability of the cell will be influenced negatively. The MEAs and the bipolar plates need to be fixed in accurate positions and the compression of gaskets needs to be safe and homogeneous. If the pressure is too high, it will cause mechanical failure of the membrane or of the bipolar plate. Furthermore, an excessive compression of the components, in particular the GDL, increases the mass transport problems with a consequent reduction of cell performance and lifetime especially at high current density. If the pressure is too low, it may cause gas or cooling fluid leakage. Another effect of low compression is the increased contact resistance between the GDL and the bipolar plate, which will result in an inhomogeneous current distribution and thus in a reduced lifetime of the MEA. Figures 6 - 16 show the stresses distribution in each component of the PEM fuel cell stack during operation.

In a conventional PEM fuel cell stack design, end plates are the two outermost components in a fuel cell assembly. They act as part of the clamping system to provide compressive force in order to unitize the single fuel cells together to form a stack. In addition, they also have some other important functions, such as ensuring good electrical contact between multiple layers within the fuel cell, ensuring good sealing at various interfaces, providing passages for the reactants, products and possibly cooling agents to enter and leave the fuel cell. Although the current design of fuel cell end plates can provide the above listed functions in a somewhat satisfactory manner, it is recognized that there are some existing problems to be solved, such as: deformation of end plates has an influence on fuel cell performance and is difficult to control; end plates are typically bulky and heavy, as compared to the fuel cell stacks; tie rods tend to loosen up during service. This may cause leakage, bad electrical contacts and deteriorated performance of the fuel cell stacks; and repeatability in pressure distribution can hardly be realized among the fuel cell stacks. The end plate material has a large influence on the mechanical properties of the end plate. A good end plate material has a high Young's modulus and a low density. Figures 6 and 16 show the von Mises stress distribution of the cathode and anode end plates respectively.

The current plate materials may influence fuel cell performance. Current plates for all kinds of fuel cell stacks are made of noble metals such as gold or platinum, or non-noble metals such as stainless steel, copper, or aluminum. The noble metals not only have good conductivity but also can almost avoid electrochemical corrosion and thus will not produce metallic ions that may poison the fuel cell. However, these noble metals are very expensive. If stainless steel, copper, or aluminum is directly used to make a current plate, electrochemical corrosion will occur if fluids pass through it, resulting in unwanted damage due to the metallic ions produced. In order to avoid this problem, nonnoble metal materials plated with gold or platinum are frequently used. Figures 7 and 15 show the von Mises stress distribution of the cathode and anode current plates respectively.

Bipolar plates have traditionally been fabricated from high-density graphite on account of its superior corrosion resistance, chemical stability, high thermal conductivity, and availability. However, due to its molecular structure, it exhibits poor mechanical properties, high manufacturing cost, and it is difficult to work with. Nevertheless, graphite has established itself as the benchmark material for fabrication of bipolar plates, against which all other materials are compared. However, it is not suitable for either transportation applications that require good structural durability against shock and vibration or large-scale manufacturing because of its poor mechanical strength. The thickness of the graphite plates cannot be reduced, resulting in bulkiness and heaviness. As a result, recent studies have moved away from graphite in the direction of developing and optimizing more cost effective materials such as metals and composites.

Metallic materials are another choice for bipolar plates because of their good mechanical strength, high electrical conductivity, high thermal conductivity, high gas impermeability, low cost, and ease of manufacturing. The most advantage of metallic bipolar plates is stampability and reducing the thickness plate. Metallic bipolar plates can significantly reduce the volume of fuel cell stacks. In addition, relatively simple fabrication process of gas channels on the metallic plates by stamping enables mass production. In spite of these technical benefits, metallic plates are highly susceptible to corrosion which is closely related to reliability and durability of fuel cell engines. Recently, polymerecarbon composite bipolar plates have been investigated due to their lower cost, less weight, and higher corrosion resistivity in comparison with available materials such as graphite or metallic bipolar plates. The disadvantages of composite bipolar plates are non-stampability, lower electrical and mechanical properties than those of metallic bipolar plates. Figures 8 and 14 show the von Mises stress distribution of the cathode and anode bipolar plate respectively.

In a fuel cell, gaskets are normally used to generate the insulation of anodic and cathodic compartments and to avoid gas cross over. Generally, they form a frame around MEA in the un-active zone of the flow

field. Because the cell plates are subject to a compression, the gasket material can influence the cell performance and durability. The use of different gasket materials changes the contact pressure distribution on the GDL, affecting the fuel cell performance and lifetime. Moreover, because of the gaskets are typically placed between the bipolar plates and the MEA to guarantee a good sealing, the chemical and mechanical characteristics and stability of the gasket materials must be investigated. In fact these properties are critical for both sealing and the electrochemical performance of the cell. Furthermore, it was found that there is an optimal difference in thickness between gaskets and GDL, in order to prevent problems related to an excessive GDL compression. Mismatch may lead to the following problems: (i) Thinner gasket may lead to sealing problem causing safety issue. In addition to that, the cell will be facing mass transport related losses. (ii) On the other hand, thicker gasket may result in poor contact between the bipolar plate and the GDL, which will be reflected on the ohmic region of the current voltage characteristics. Figures 9 and 13 show the von Mises stress distribution of the cathode and anode gaskets respectively.

One of the key elements affecting PEM fuel cell stack performance is the GDL, which must provide a passage for reactant access and excess product removal to/from the catalyst layers, high electronic and thermal conductivity, and adequate mechanical support for the MEA. In order to fulfill these requirements, GDLs are typically made of highly porous carbon-fiber paper or cloth. The high porosity of these materials provides to the GDL a characteristic soft and flexible structure, susceptible of large deformations when subjected to compression. This leads to significant changes in its mechanical, electrical and thermal properties (thickness, porosity, permeability, electrical and thermal bulk conductivities and contact resistances, etc.), thus affecting mass, charge, and heat transfer processes, fuel cell performance and lifetime.

Each type of GDL material has its own optimal clamping pressure, to achieve a proper and uniform pressure distribution inside the stack. The inhomogeneous compression of the GDL leads to several opposing effects. On one hand, the assembly pressure improves both electric and thermal conductivities by reducing bulk and contact resistances. Slight compressions may also reduce mass transport resistance due to the shortening of the diffusion path to be covered by the reactants and products in their way to/from the catalyst layers. However, excessive compression loads may impede reactant and product transport due to the loss of pore volume, which is typically, accompanied by a reduction of the effective species diffusivities. On top of that, excessive assembly pressures are known to damage typical paper type GDLs, induce local delamination of the GDL under the channel, and result in non-uniform compressive loads which may degrade the membrane. Pore size reduction may also affect multiphase capillary transport phenomena in the GDL (liquid water removal in PEM fuel cells). And last, but not least, partial GDL intrusion into the channel produces a reactant flow rate reduction or, alternatively, an increase of the parasitic power required to maintain the flow, which affects the overall efficiency of the stack.

In the operation PEM fuel cell, the contact pressure on the GDL is increased because of the thermal expansion of cell materials and membrane swelling. Furthermore, due to the round corners of the bipolar plate, the contact behavior at the interface is hard to predict without a CFD analysis. Figures 10 and 12 show the von Mises stress distribution of the cathode and anode GDLs respectively.

The heart of a fuel cell is a polymer, proton exchange membrane (PEM). On both sides of the membrane there are catalyst layer. Mechanical stresses which limit MEA durability have two origins. Firstly, this is the stresses arising during fuel cell assembly (bolt assembling). The bolts provide the tightness and the electrical conductivity between the contact elements. Secondly, additional mechanical stresses occur during fuel cell running because PEM fuel cell components have different thermal expansion and swelling coefficients. Thermal and humidity gradients in the fuel cell produce dilatations obstructed by tightening of the screw-bolts. Compressive stress increasing with the hygro-thermal loading can exceed the yield strength which causes the plastic deformation. The mechanical behavior of the membrane depends strongly on clamping pressure, hydration and temperature. Furthermore, in an operating fuel cell, because the four sides of the membranes are fixed, variations in temperature and humidity during operation can induce MEA dimensional change and corresponding cyclic stresses and strains inside it. Mechanical MEA degradation can occur in many forms, such as MEA thinning, tears, cracks, pinholes, and so on. Figure 11 shows the von Mises stress distribution of the MEA.

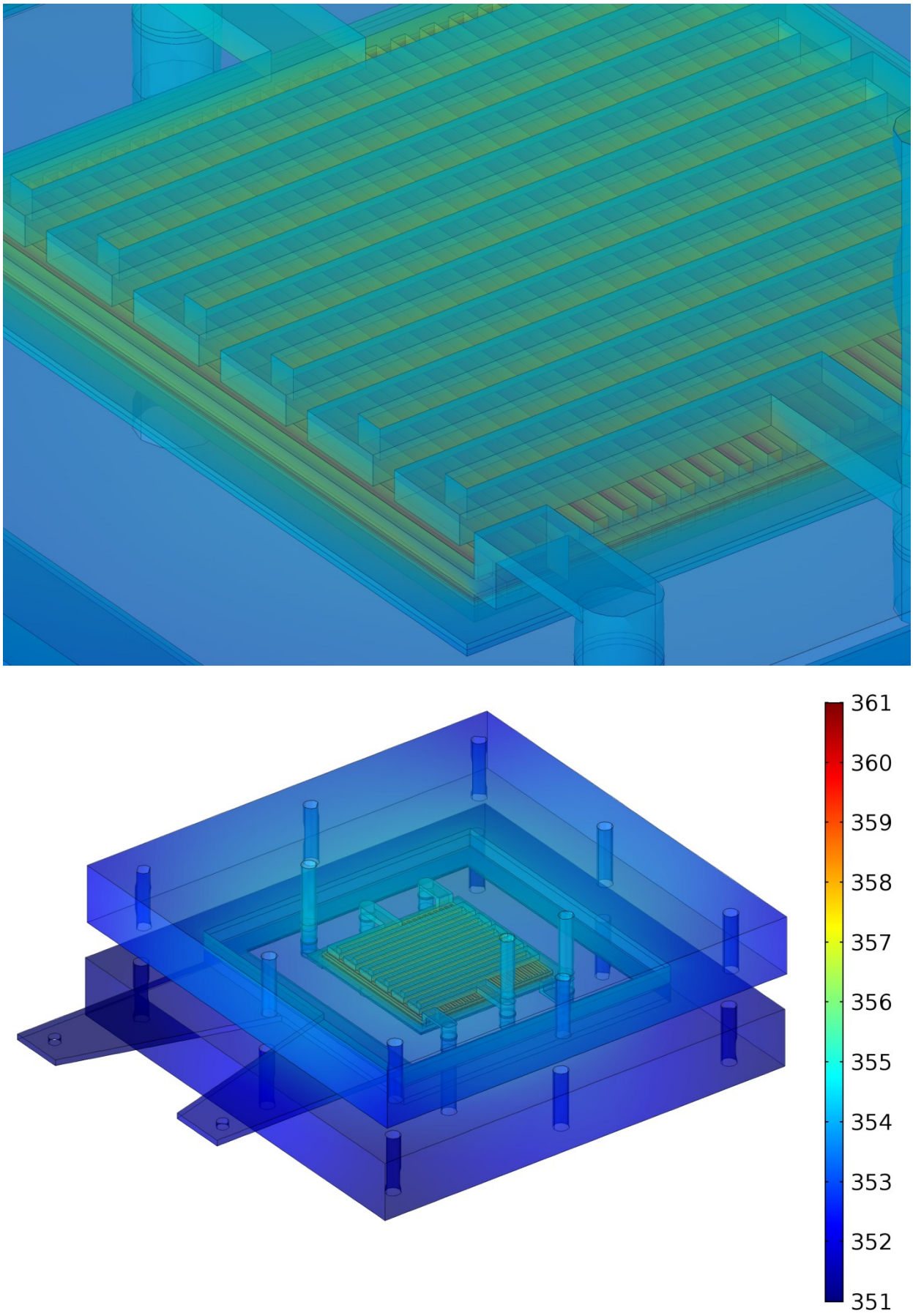

Figure 4. Solid-phase temperature distribution in the PEM fuel cell stack during operation [K].

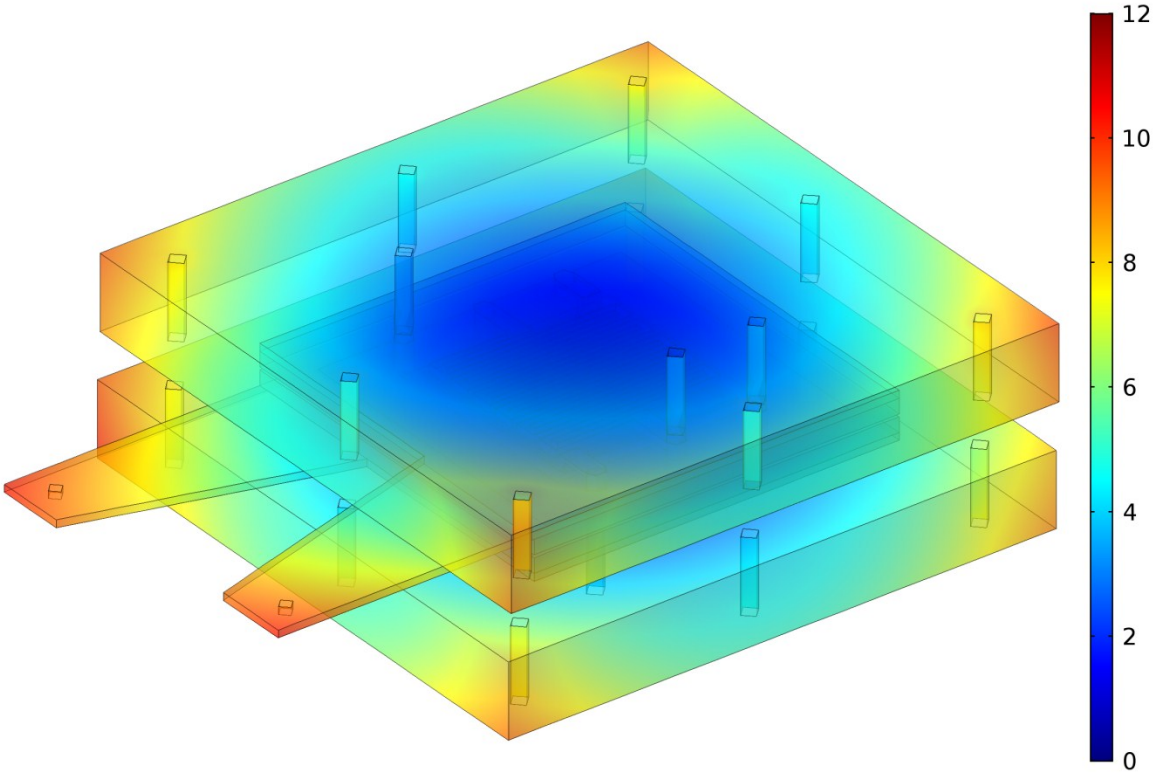

(a) during assembly process.

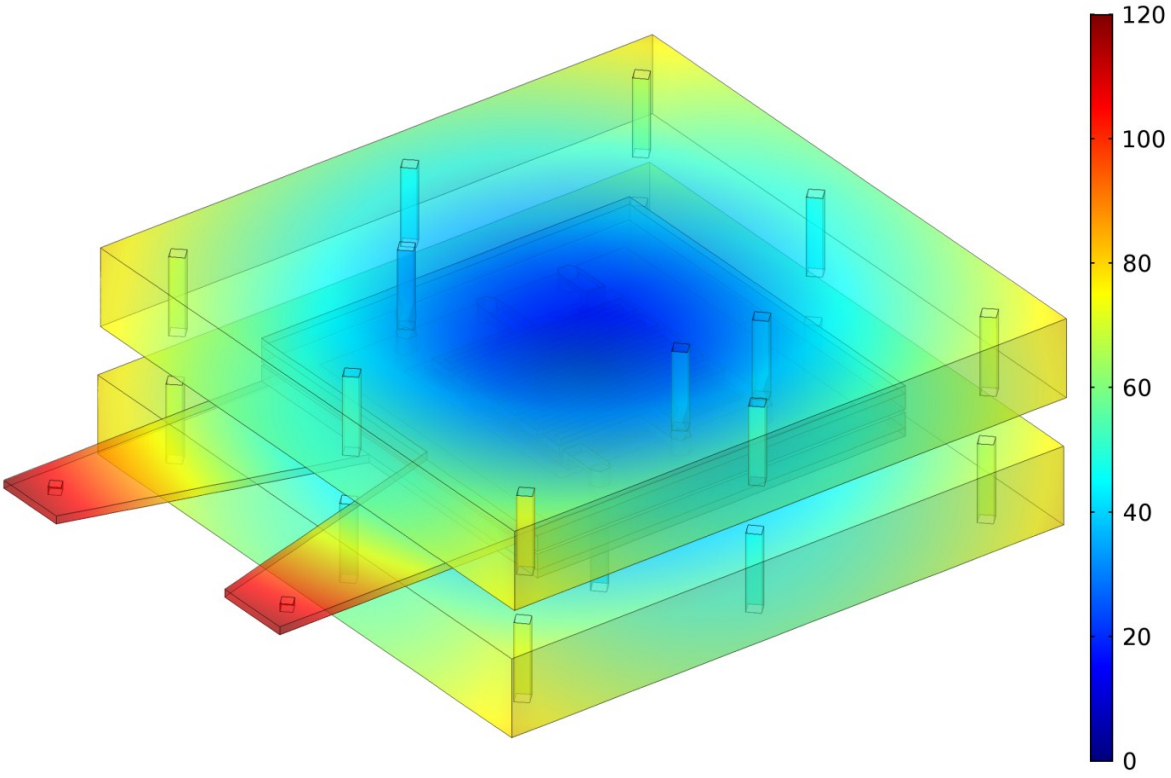

(b) during operation.

Figure 5. Total displacement distribution in the PEM fuel cell stack [μm].

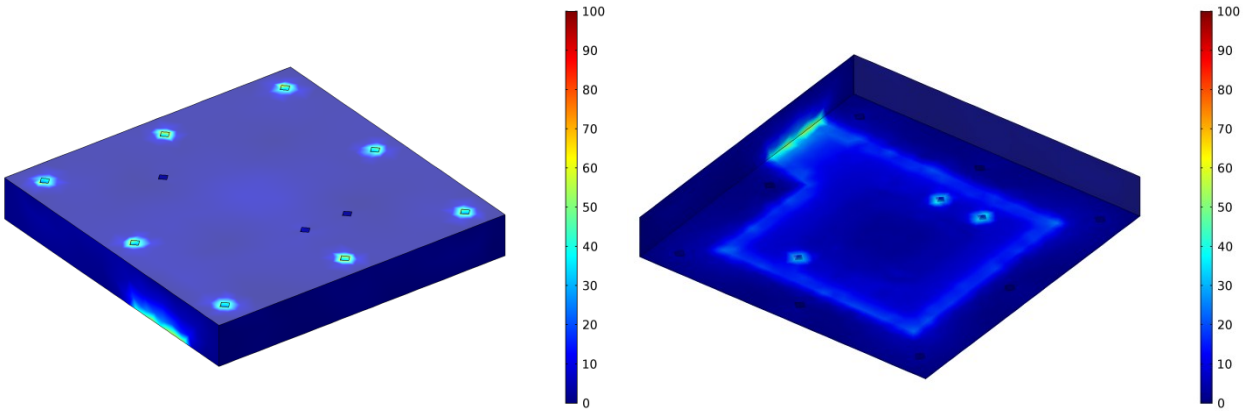

View from the top View from the bottom

Figure 6. Cathode end plate von Mises stress distribution [MPa].

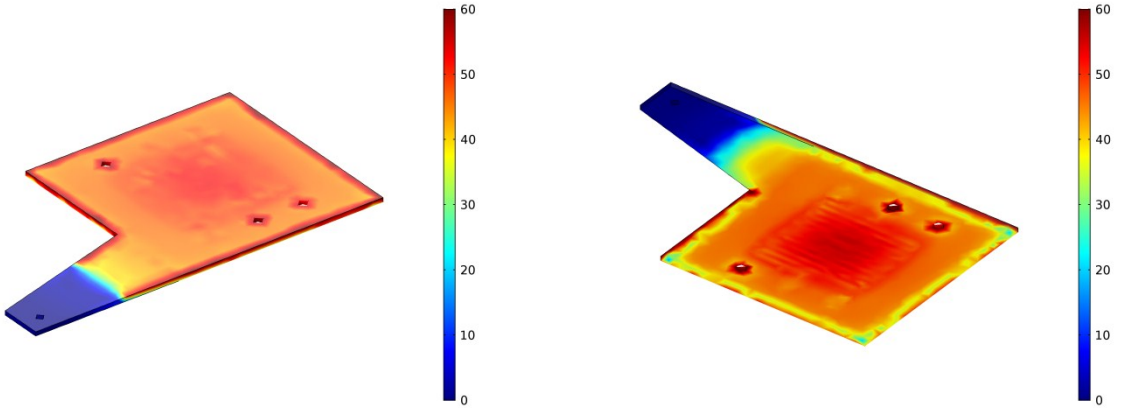

View from the top View from the bottom

Figure 7. Cathode current plate von Mises stress distribution [MPa].

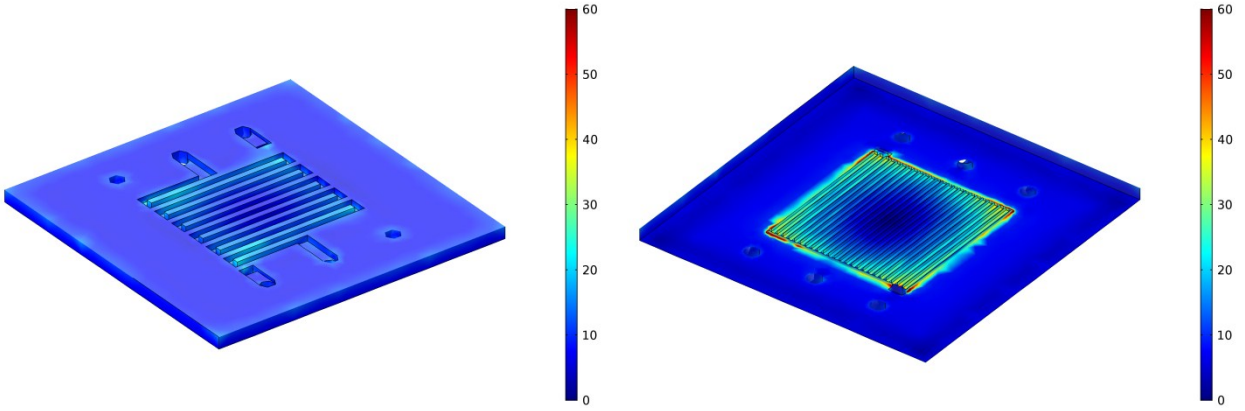

View from the top View from the bottom

Figure 8. Cathode bipolar plate von Mises stress distribution [MPa].

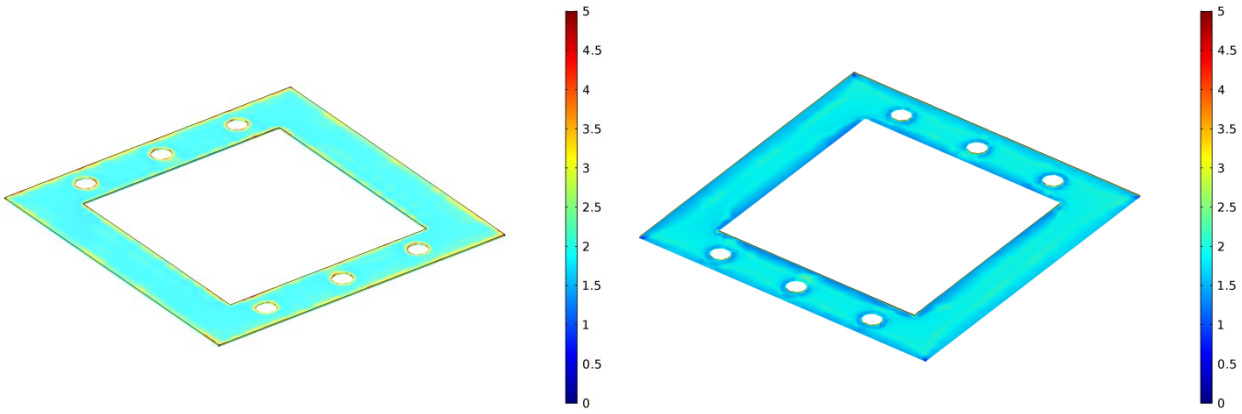

View from the top View from the bottom

Figure 9. Cathode gasket von Mises stress distribution [MPa].

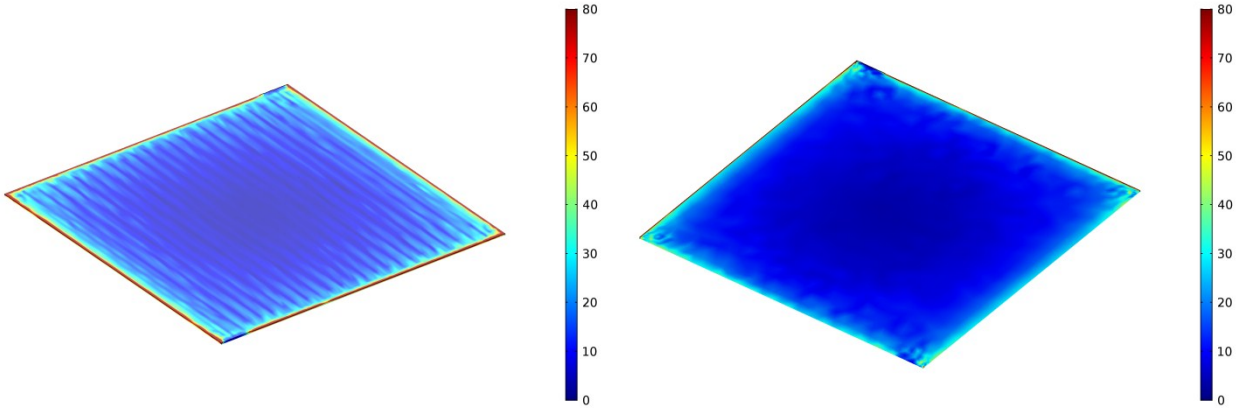

View from the top View from the bottom

Figure 10. Cathode GDL von Mises stress distribution [MPa].

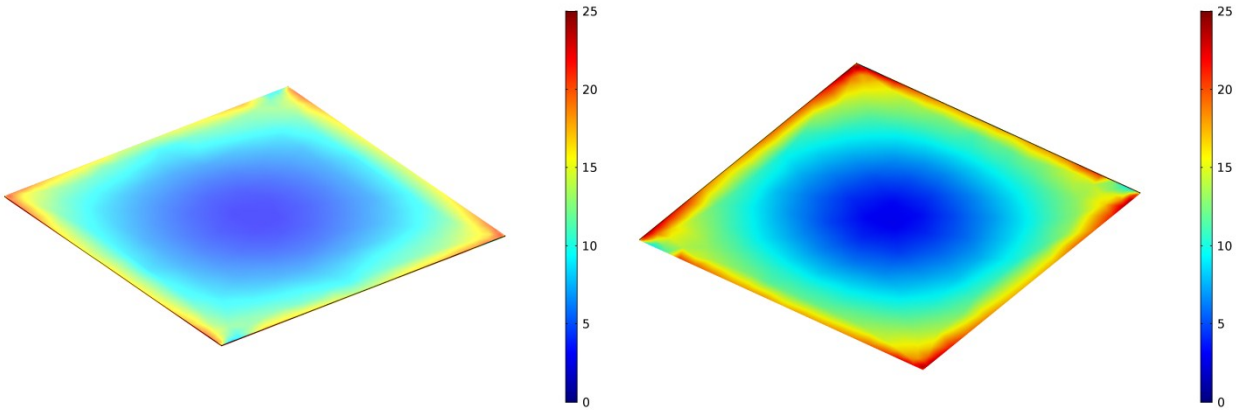

View from the top View from the bottom

Figure 11. MEA von Mises stress distribution [MPa].

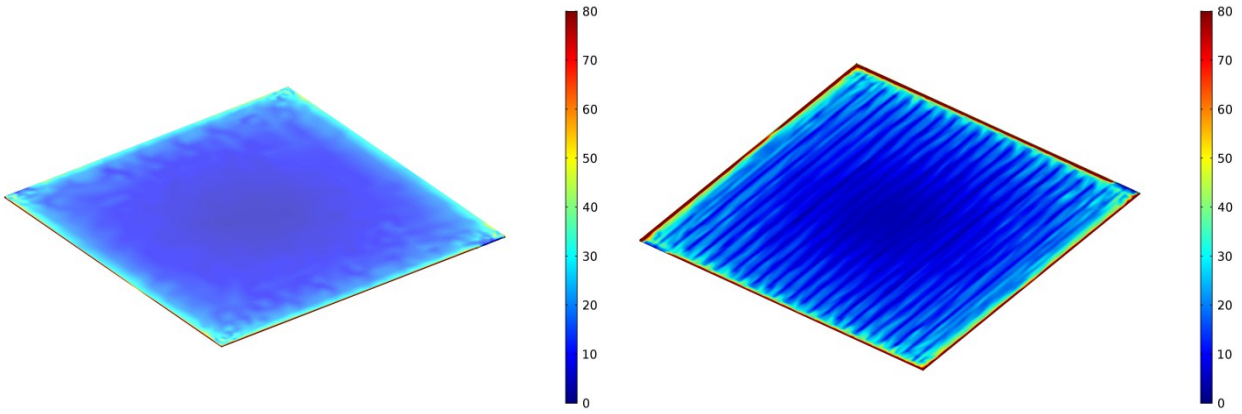

View from the top View from the bottom

Figure 12. Anode GDL von Mises stress distribution [MPa].

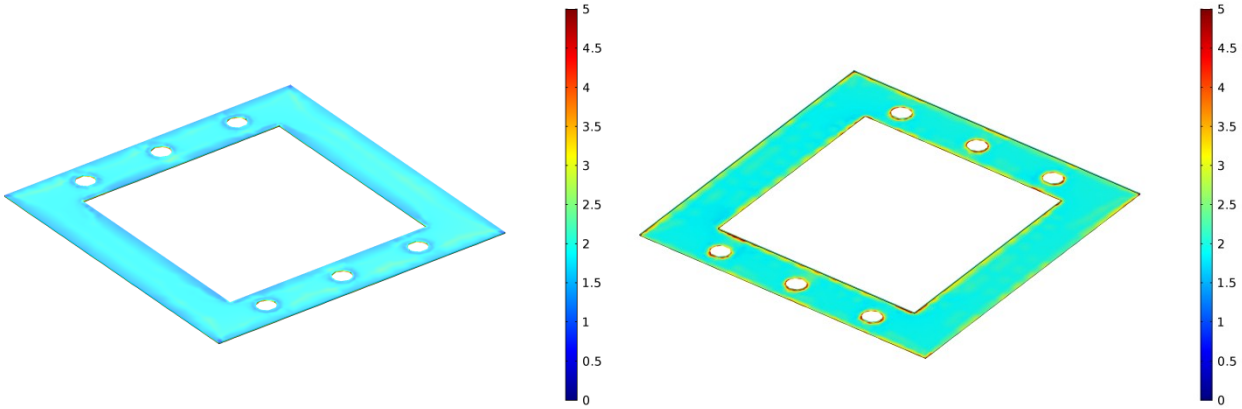

View from the top View from the bottom

Figure 13. Anode gasket von Mises stress distribution [MPa].

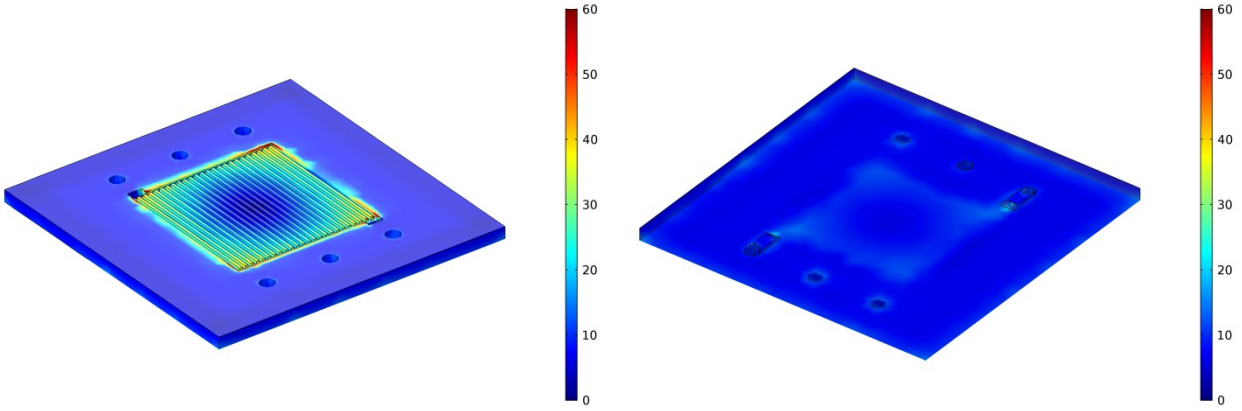

View from the top View from the bottom

Figure 14. Anode bipolar plate von Mises stress distribution [MPa].

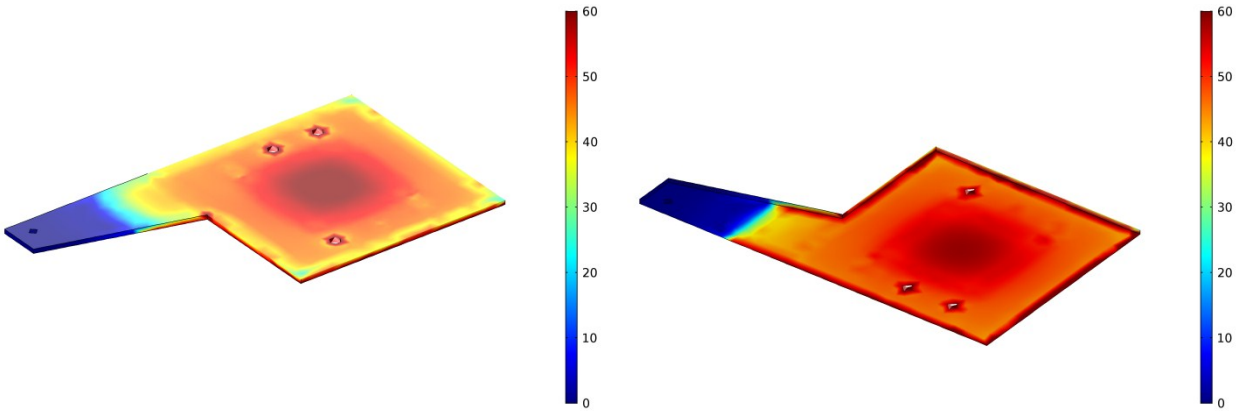

View from the top View from the bottom

Figure 15. Anode current plate von Mises stress distribution [MPa].

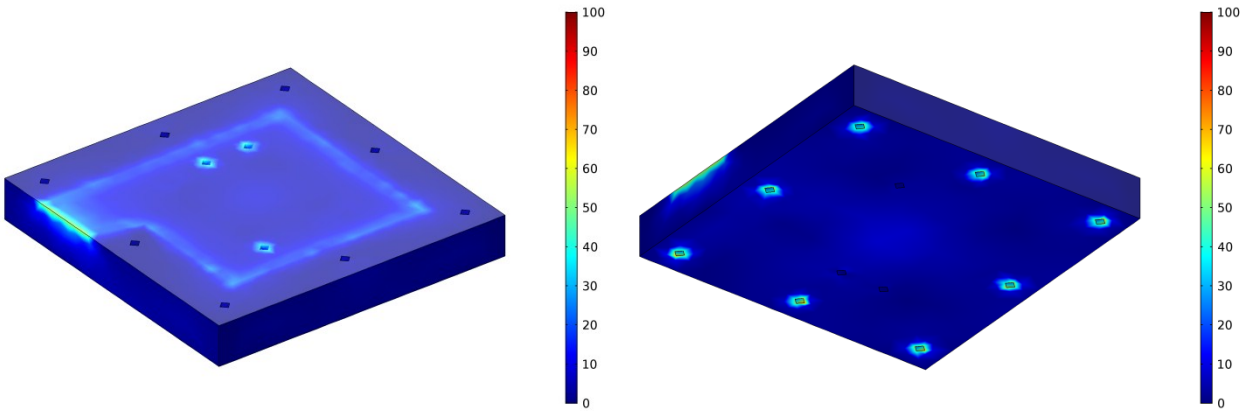

View from the top View from the bottom

Figure 16. Anode end plate von Mises stress distribution [MPa].

4. Conclusion

This work develops a three dimensional non-isothermal CFD model to study the pressure effects by combining the mechanical and electrochemical phenomena in PEM fuel cells stack. Solid mechanics-CFD simulation of a single PEM fuel cell stack, integrating the real full scale geometry of all components, was successful and has not been previously seen in literatures work. The simulation shown here provides a 3D analysis of stress distribution in all materials of a fuel cell stack during operation. The present numerical study provides a fundamental understanding of the stress-temperature-swelling interaction during PEM fuel cell stack operations and demonstrates that the coupled solid mechanics/CFD PEM fuel cell stack model presented in this work can be used as a useful tool for optimizing PEM fuel cell stack clamping and operating conditions. This model is an important step for further development of the stack design and the flow field of a PEM fuel cell stack.

Acknowledgements

This work was supported by International Energy and Environment Foundation (IEEF).

References

[1] Maher A.R. Sadiq Al-Baghdadi. PEM Fuel Cells-from Single Cell to Stack: Fundamentals, Modeling, Analysis, and Applications. International Energy and Environment Foundation, 2015.

[2] Maher A.R. Sadiq Al-Baghdadi. Proton exchange membrane fuel cells modeling: A review of the last ten years results of the Fuel Cell Research Center-IEEF. International Journal of Energy and Environment 2017, 8(1); pp.1-28.

[3] Maher A.R. Sadiq Al-Baghdadi. Modeling optimizes PEM fuel cell durability using three-dimensional multi-phase computational fluid dynamics model. International Journal of Energy and Environment. 2010, 1(3); pp. 375-398.

[4] Maher A.R. Sadiq Al-Baghdadi. Prediction of deformation and hygro-thermal stresses distribution in PEM fuel cell vehicle using three dimensional CFD model. International Journal of Energy and Environment IJEE, 2012; 3(4), 485-504.

[5] Zhang, S.; Yuan, X.; Wang, H.; Merida, W.; Zhu, H.; Shen, J.; Wu, S.; Zhang, J. A review of accelerated stress tests of MEA durability in PEM fuel cells. Int. J. Hydrogen Energy, 2009; 34(1): 388-404.

[6] Wu, J.; Yuan, X.Z.; Martin, J.J.; Wang, H.; Zhang, J.; Shen, J.; Wu, S.; Merida, W. A review of PEM fuel cell durability: Degradation mechanisms and mitigation strategies. J. Power Sources, 2008; 184(1): 104-119.

[7] Y. Hung, H. Tawfik, D. Mahajan. Durability and characterization studies of polymer electrolyte membrane fuel cell's coated aluminum bipolar plates and membrane electrode assembly. Journal of Power Sources 2009, 186, pp.123–127.

[8] Marrony, M.; Barrera, R.; Quenet, S.; Ginocchio, S.; Montelatici, L.; Aslanides, A. Durability study and lifetime prediction of baseline proton exchange membrane fuel cell under severe operating conditions. J. Power Sources, 2008; 182(2), pp.469-475.

[9] Ramaswamy, N.; Hakim, N.; Mukerjee, S. Degradation mechanism study of perfluorinated proton exchange membrane under fuel cell operating conditions. Electrochimica Acta 2008; 53(8): pp.3279-3295.

[10] Christophe Carral, Nicolas Charvin, Helene Trouve, Patrice Mele. An experimental analysis of PEMFC stack assembly using strain gage sensors. Int.J.Hydrogen Energy 2014, 39, pp.4493-4501.

[11] I. Gatto, F. Urbani, G. Giacoppo, O. Barbera, E. Passalacqua. Influence of the bolt torque on PEFC performance with different gasket materials. Int. J. Hydrogen Energy 2011, 36, pp.13043-13050.

[12] Thomas J. Mason, Jason Millichamp, Tobias P. Neville, Ahmad El-kharouf, Bruno G. Pollet, Daniel J.L. Brett. Effect of clamping pressure on ohmic resistance and compression of gas diffusion layers for polymer electrolyte fuel cells. Journal of Power Sources 2012, 219, pp.52-59.

[13] Debanand Singdeo, Tapobrata Dey, Prakash C. Ghosh. Contact resistance between bipolar plate and gas diffusion layer in high temperature polymer electrolyte fuel cells. Int. J. Hydrogen Energy 2014, 39, 987-995.

[14] Pucheng Pei, Huicui Chen. Main factors affecting the lifetime of Proton Exchange Membrane fuel cells in vehicle applications: A review. Applied Energy 2014, 125, 60-75.

[15] C. Totzke, G. Gaiselmann, M. Osenberg, J. Bohner, T. Arlt, H. Markotter, A. Hilger, F. Wieder, A. Kupsch, B.R. Muller, M.P. Hentschel, J. Banhart, V. Schmidt, W. Lehnert, I. Manke. Three-dimensional study of compressed gas diffusion layers using synchrotron X-ray imaging. Journal of Power Sources 2014, 253, pp.123-131.

[16] Kyung Don Baik, Bo Ki Hong, Kookil Han, Min Soo Kim. Effects of anisotropic bending stiffness of gas diffusion layers on the performance of polymer electrolyte membrane fuel cells with bipolar plates employing different channel depths. Renewable Energy 2014, 69, pp.356-364.

[17] Dong-hao Ye, Zhi-gang Zhan. A review on the sealing structures of membrane electrode assembly of proton exchange membrane fuel cells. Journal of Power Sources 2013, 231, pp.285-292.

[18] Kusoglu, A.; Karlsson, A.M., Santare, M.H.; Cleghorn, S.; Johnson, W.B. Mechanical behavior of fuel cell membranes under humidity cycles and effect of swelling anisotropy on the fatigue stresses. J. Power Sources, 2007; 170(2), pp.345-358.

[19] Solasi, R.; Zou, Y.; Huang, X.; Reifsnider, K.; Condit, D. On mechanical behavior and in-plane modeling of constrained PEM fuel cell membranes subjected to hydration and temperature cycles. J. Power Sources, 2007; 167(2), pp.366-377.

[20] Bograchev, D.; Gueguen, M.; Grandidier, J-C.; Martemianov, S. Stress and plastic deformation of MEA in fuel cells stresses generated during cell assembly.J.PowerSources,2008;180(2):393-401.

[21] Suvorov, A.P.; Elter, J.; Staudt, R.; Hamm, R.; Tudryn, G.J.; Schadler, L.; Eisman, G. Stress relaxation of PBI based membrane electrode assemblies. Int. J. Solids and Structures, 2008; 45(24): 5987-6000.

[22] Tang, Y.; Kusoglu, A.; Karlsson, A.M.; Santare, M.H.; Cleghorn, S.; Johnson, W.B. Mechanical properties of a reinforced composite polymer electrolyte membrane and its simulated performance in PEM fuel cells. J. Power Sources, 2008; 175(2), pp.817-825.

[23] Bograchev, D.; Gueguen, M.; Grandidier, J-C.; Martemianov, S. Stress and plastic deformation of MEA in running fuel cell. Int. J. Hydrogen Energy, 2008; 33(20), pp.5703–5717.

[24] Y. Zhou, G. Lin, A.J. Shih, S.J. Hu. Assembly pressure and membrane swelling in PEM fuel cells. Journal of Power Sources 2009; 192, pp.544–551.

[25] Y. Zhou, G. Lin, A. J. Shih, S. J. Hu. Multiphysics Modeling of Assembly Pressure Effects on Proton Exchange Membrane Fuel Cell Performance. Journal of Fuel Cell Science and Technology, ASME 2009, 6, pp.041005-1-7.

[26] Pablo A. Garcıa-Salaberri, Marcos Vera, Ramon Zaera. Nonlinear orthotropic model of the inhomogeneous assembly compression of PEM fuel cell gas diffusion layers. Int. J. Hydrogen Energy 2011; 36, pp.11856-11870.

[27] Purushothama Chippar, Kyeongmin Oh, Dongmin Kim, Tae-Whan Hong, Whangi Kim, Hyunchul Ju. Coupled mechanical stress and multi-dimensional CFD analysis for high temperature proton exchange membrane fuel cells (HT-PEMFCs). Int. J. Hydrogen Energy 2013; 38, pp.7715-7724.

[28] Yibo Zhou, Kui Jiao, Qing Du, Yan Yin, Xianguo Li. Gas diffusion layer deformation and its effect on the transport characteristics and performance of proton exchange membrane fuel cell. Int. J. Hydrogen Energy 2013; 38, pp.12891-12903.

[29] Qinghui Hu, Dongming Zhang, Hao Fu, KaiKai Huang. Investigation of stamping process of metallic bipolar plates in PEM fuel celldNumerical simulation and experiments. Int. J. Hydrogen Energy 2014; 39, pp.13770-13776.

[30] Kyeongmin Oh, Purushothama Chippar, Hyunchul Ju. Numerical study of thermal stresses in hightemperature proton exchange membrane fuel cell (HT-PEMFC). Int. J. Hydrogen Energy 2014; 39, pp.2785-2794.

[31] Maher A.R. Sadiq Al-Baghdadi. A CFD study of hygro-thermal stresses distribution in PEM fuel cell during regular cell operation. Renewable Energy 2009, 34(3); pp.674-682.

[32] Christophe Carral, Patrice Mele. A numerical analysis of PEMFC stack assembly through a 3D finite element model. Int. J. Hydrogen Energy 2014; 39, pp.4516-4530.

[33] Alex Bates, Santanu Mukherjee, Sunwook Hwang, Sang C. Lee, Osung Kwon, Gyeung Ho Choi, Sam Park. Simulation and experimental analysis of the clamping pressure distribution in a PEM fuel cell stack. Int. J. Hydrogen Energy 2013; 38, pp.6481-6493.

[34] Javier de la Cruz, Ulises Cano, Tatiana Romero. Simulation and in situ measurement of stress distribution in a polymer electrolyte membrane fuel cell stack. Journal of Power Sources 2016; 329, pp.273-280.

[35] Willy Charon, Marie-Christine Iltchev, Jean-Francois Blachot. Mechanical simulation of a Proton Exchange Membrane Fuel Cell stack using representative elementary volumes of stamped metallic bipolar plates. Int. J. Hydrogen Energy 2014; 39, pp.13195-13205.

[36] Chi-Hui Chien, Yao-Lun Hu, Ting-Hsuan Su, Hsuan-Ting Liu, Chung-Ting Wang, Ping-Feng Yang, Ying-Xu Lu. Effects of bolt pre-loading variations on performance of GDL in a bolted PEMFC by 3-D FEM analysis. Energy 2016; 113, pp.1174-1187.

[37] Berning, T.; Djilali, N. A 3D, multi-phase, multicomponent model of the cathode and anode of a PEM fuel cell. J. Electrochem. Soc., 2003; 150(12): A1589-A1598.

[38] Maher A.R. Sadiq Al-Baghdadi. Novel design of a compacted micro-structured air-breathing PEM fuel cell as a power source for mobile phones. International Journal of Energy and Environment 2010, 1(4); pp.555-572.

[39] Maher A.R. Sadiq Al-Baghdadi. Modelling of proton exchange membrane fuel cell performance based on semi-empirical equations. Renewable Energy 2005, 30(10); pp.1587-1599.

